

# Time-dependent tomography of heliospheric features using the three dimensional reconstruction techniques developed for the Solar Mass Ejection Imager (SMEI)

Bernard V. Jackson<sup>\*</sup>, P. Paul Hick<sup>\*\*</sup> and A. Buffington<sup>\*\*\*</sup>

Center for Astrophysics and Space Sciences, University of California at San Diego

## ABSTRACT

Precise photometric images of the heliosphere are expected from the Air Force/NASA Solar Mass Ejection Imager (SMEI) now scheduled for launch in February 2003, and the all-sky cameras proposed for other NASA missions. To optimize the information available from these instruments, we are developing tomographic techniques for analyzing remote sensing observations of heliospheric density as observed in Thomson scattering (*e.g.* using the Helios photometer data) for eventual use with SMEI. We have refined the tomography program to enable us to analyze time-dependent phenomena, such as the evolution of corotating heliospheric structures and more discrete events such as coronal mass ejections. Both types of phenomena are discerned in our data, and are reconstructed in three dimensions. We use our tomography technique to study the interaction of these phenomena as they move outward from the Sun for several events that have been studied by multiple spacecraft *in situ* observations and other techniques.

**Key words:** Coronal mass ejections, CME-corotating region interactions, tomography, three-dimensional reconstructions

## 1. INTRODUCTION

There have been numerous attempts to reconstruct coronal structures in the corona and heliosphere in three dimensions. These techniques, reviewed elsewhere<sup>1,2</sup>, have been motivated by attempts to determine heliospheric structure morphology in order to determine their physics, their dynamics and most recently to forecast their arrival at Earth using remote sensing techniques.

Rotational tomography of stationary solar structures (streamers) using coronagraph observations have been presented by Wilson<sup>3</sup>, Jackson<sup>4</sup>, and by Zidowitz *et al.*<sup>5</sup>. More recently, Jackson *et al.*<sup>6-8</sup> presented results that show heliospheric 3-dimensional reconstructions from outward plasma flow alone. These “time-dependent” tomographic analyses have been used to determine and successfully forecast the Earth arrival of both heliospheric corotating structures and mass ejections from ground-based interplanetary scintillation (IPS) observations and the Helios photometer data. The same techniques, used with a sufficiently sensitive photometer-type imaging system on a three-axis stabilized spacecraft, can give context to *in situ* spacecraft measurements and can view plasma structures long before they arrive at the spacecraft. Here we illustrate this using Thomson-scattering observations from the Helios spacecraft photometers.

The Helios spacecraft, launched in December 1974 (Helios 1) and January 1976 (Helios 2), each contained three zodiacal light photometers which were originally intended to measure the distribution of dust in the interplanetary medium between the Sun and the Earth<sup>9,10</sup>. However, these photometers could also measure brightness variations produced by large-scale differences in the interplanetary electron content (Fig. 1). The three photometers were fixed on the spacecraft and rotated at its 1 s spin period on an axis perpendicular to the plane of the ecliptic; they pointed 16°, 31° and 90° north or south of the ecliptic plane. Data from the 16° and 31° photometers were binned into 32 longitude sectors at constant ecliptic latitude around the sky. The photometer data were integrated over 8.6-min periods in turn from each of the three photometers through a set of broad-band ultraviolet, blue, and visual light filters and a set of one clear and three polarizing filters with a time interval of about 5 hours between the same filter combinations.

Richter *et al.*<sup>11</sup> first described the use of these data to follow plasma ejections detected by electron Thomson scattering out to  $\epsilon = 90^\circ$  solar elongation (angular distance from the Sun). Since then Jackson and Leinert<sup>12</sup> and Jackson<sup>13</sup> have used the Helios photometer data to study the characteristics of mass ejections and have traced their motion outward from the Sun into the anti-solar hemisphere. Jackson<sup>14</sup> has also used the Helios photometer data to study the longer-lasting corotating regions in the solar wind. Because the two Helios spacecraft orbited the Sun with 6-month periods from 0.3 to 1 A.U., the photometers viewed heliospheric structures from a non-Earth perspective. The photometer data can also be used to construct tomographic models of the electron densities required to provide the observed brightness.

The next section describes the tomographic program developed to fit the Helios spacecraft photometer brightness. The third section gives examples of this analysis and compares these tomographic models to Helios *in situ* observations and to simultaneous coronagraph observations of a CME. We conclude in the last section.

## 2. TOMOGRAPHIC ANALYSIS – THEORY AND MODELING

Line-of-sight Thomson scattering brightnesses for a column of electrons follow the relationship,

$$B = \int n_e(s)W(s)ds, \quad (1)$$

where  $n_e(s)$  is the electron density at distance  $s$  along the line of sight and  $W(s)$  is a ‘weight factor’. For the large distances from the Sun viewed by the Helios photometers,

$$W(s) = \frac{1}{2} \sigma F_s \left( \frac{r_0}{r} \right)^2 (2 - \sin^2 \chi), \quad (2)$$

where  $\sigma$  is the Thomson-scattering cross section,  $F_s$  the flux received from the solar disk at a distance  $r_0$ ,  $r$  is the distance of the electron from the Sun, and  $\chi$  is the angle between the incident radiation from the Sun and the direction of scattering as in Billings<sup>15</sup>. To evaluate Eq. (1) both  $r$  and  $\chi$  are expressed as functions of the distance  $R$  of the observer from the Sun, the elongation  $\mathcal{E}$  of the line of sight and the distance  $s$  along the line of sight.  $W$  scales as  $R^{-2}$ . For  $\mathcal{E} < 90^\circ$   $W$  peaks at  $s = R \cos \mathcal{E}$ , the distance of closest approach to the Sun. Fig. 2 shows the weight function for elongations  $16^\circ$ ,  $31^\circ$  and  $90^\circ$  at a Sun-observer distance of 1 AU.

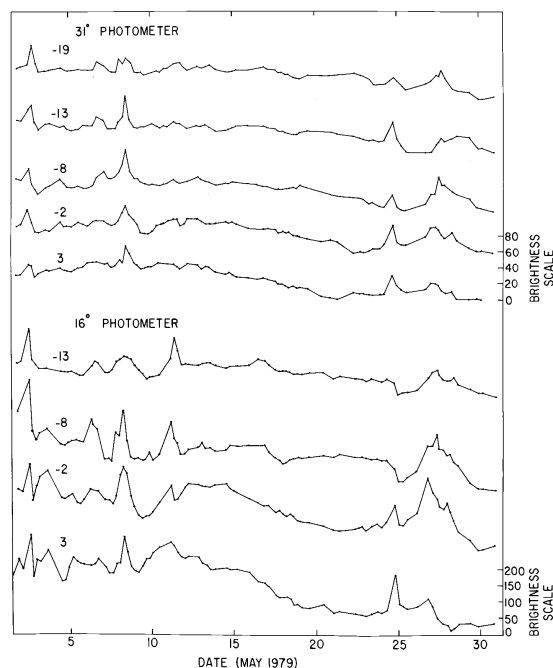


Fig. 1: Helios 2 time series data for the month of May, 1979. Most of the large, slowly varying zodiacal light component has been removed from the data. The  $16^\circ$  and  $31^\circ$  photometer sectors with centers at ecliptic longitudes of  $3^\circ$ ,  $-2^\circ$ ,  $-8^\circ$ , and  $-13^\circ$  relative to the Sun in visual light are shown. An additional  $31^\circ$  sector time series at  $-19^\circ$  is also shown. The May 7 CME discussed in the following text can be observed along with other heliospheric variations in the data as a bright peak in both photometers ~May 8.

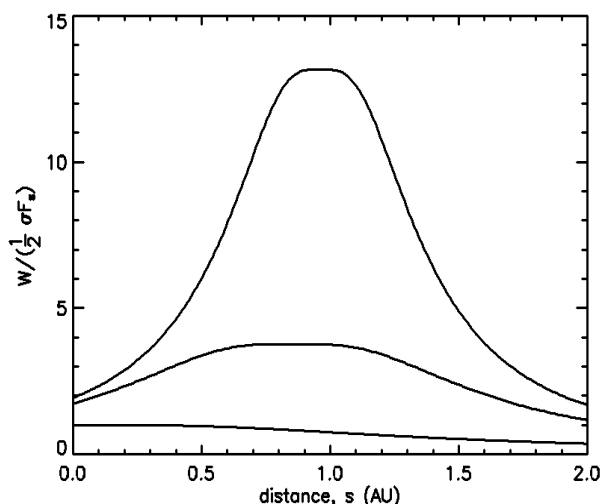


Fig. 2: Thomson-scattering weight function  $W$  from Eq. (2) as a function of distance  $s$  along the line of sight for elongations of  $16^\circ$  (top curve),  $31^\circ$  (center) and  $90^\circ$  (bottom). The observer is assumed to be at  $R = 1$  AU from the Sun.

The Helios photometer brightness data are usually provided in S10 units, the brightness equivalent to one tenth-magnitude solar-type star in degree of sky. Expressing Eq. (1) and Eq. (2) in S10 units requires that the flux  $F_s$  received from the Sun [Eq. (2)] is also specified in S10 units:

$$\frac{1}{2}\sigma F_s = \frac{1}{2}\sigma(\Delta\Gamma/\Omega_s)10^{(10-m)/2.5} = 8.76\times 10^{-11}cm^2S10. \quad (3)$$

where  $\Delta\Gamma$  is the solid angle subtended by one square degree of sky, and  $\Omega_s$  and  $m$  are the solid angle and the apparent magnitude of the Sun. At 1 AU  $m = -26.73$ , and thus  $1/2\sigma F_s$  is the value specified in Eq. (3) with  $s$  in cm.

The UCSD tomography program<sup>1</sup> applies corrections to a kinematic model, modifying the model until there is a least squares best fit match with the observations. Density and velocity are projected outward from a lower boundary (source surface) below the lowest lines of sight. Consistent approximately with *in situ* spacecraft observations, the solar wind motion is assumed to be radial outward from this surface. Thus, for example, when faster solar wind catches up with slower wind, the resultant solar wind speed is continued after merging by assuming that both mass and mass flux are conserved within the latitudinal band resolved by the model. In the kinematic model described here, the inputs at the lower boundary can change over time intervals from a few days to as short as a few hours. This assumption essentially limits the tomographic reconstruction to rely on outward solar wind flow to form the perspective views. For each observed line of sight at a given time, the position along this line in the model is calculated. The model density along each line of sight is summed using the weighting mentioned in Eq. 2 to obtain brightness. These model values are then compared with the observed brightness, and this comparison is used to change the model at the source surface. For one solar rotation typically 5000 to 10000 lines of sight can be used to determine model density from the brightness measurements. This implies 200 and 400 line of sight components on the lower source surface boundary contribute to latitude and longitude changes in density each day. This implies the possibility of determining the density for 200 to 400 latitude and longitude locations each day.

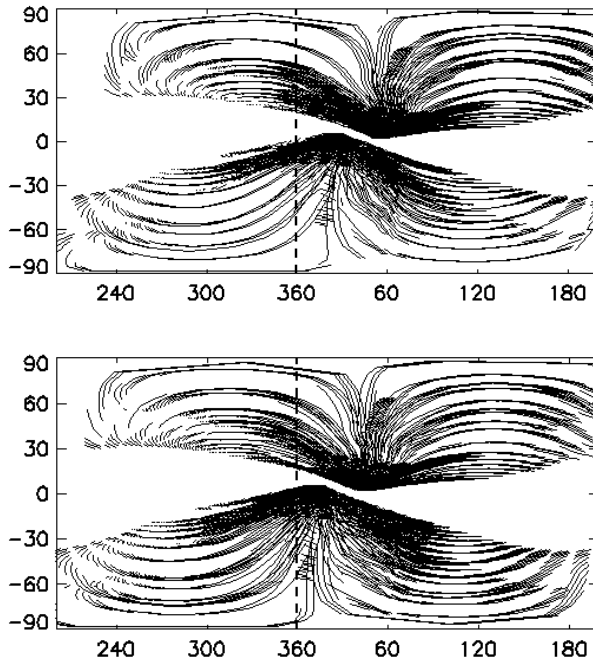


Fig. 3: Consecutive-day (November 21 and 22, 1977) latitude and longitude line of sight projections onto the source surface. Lines of sight extend outward from spacecraft for 2 times the distance of the spacecraft from the Sun beginning near the projected sub-spacecraft point at the center of the map. Some lines of sight complete their projection on adjacent days. Perspective views are realized from the different weights on the source surface maps at each latitude and longitude.

For the UCSD time dependent tomographic program using Helios photometer data,  $10^\circ$  by  $10^\circ$  heliographic latitude and longitude resolution is used and a one day cadence. The regions near the spacecraft are those most frequently crossed by different lines of sight while those far from them are not. Helios 1 looks to the south of the ecliptic and Helios 2 looks north. This is shown in Fig. 3 for two consecutive days during a period in November 1977. The reference surface maps are smoothed each iteration using a Gaussian spatial filter that incorporates equal solar surface areas and a Gaussian temporal filter. At the reference surface the velocity structure of the model is smoothed using a Gaussian filter weighted according to the angular distance of the adjacent resolution elements on this surface. Since the resolution of rectangular Carrington coordinate maps increase in longitude with increasing latitude, this filter is used to even the spatial resolution over the whole map. These spatial and temporal filters can be varied to insure convergence. Filter changes by large amounts (factors of two) have a significant effect

on the smoothness of the result. The Gaussian filter parameters for the Helios observations are typically set to a  $1/e$  width of  $7.0^\circ$  and 0.8 days, for the  $10^\circ$  by  $10^\circ$  and 1-day model digitization. In practice, lines of sight often extend over several consecutive time steps. The amount and quality of the observations dictate even more strongly the resolution that can be used.

Convergence using IPS velocity is another matter. During the years of Helios spacecraft operation some UCSD IPS velocity data were available. These amounted to at most three or four observations per day. Like the UCSD IPS time dependent tomography<sup>8</sup> this tomographic program can use this information (at a low spatial and temporal cadence compared with the Helios data) to converge to a solution. Typically an 8-day temporal cadence is used, and with the same digital latitude and longitude digitization as the Helios data, a Gaussian temporal filter of about 5 days and a spatial filter of  $15^\circ$  are incorporated. When no IPS velocity data are available or these data are too sparse, the velocity at the lower source surface boundary can be assumed constant or can be approximated assuming  $mv^2 = \text{constant}$ .

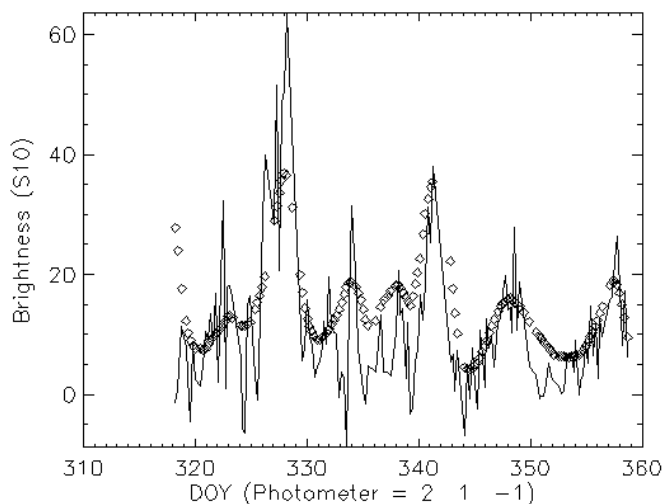


Fig. 4: Time series showing a sample of the final (18<sup>th</sup> iteration) model and photometer brightness comparison for a time-dependent tomographic run for Helios November, 1977 data. The observed brightness is shown as a solid line; the model brightness as open circles. The Helios 2  $16^\circ$  photometer viewing  $2^\circ$  west of the Sun-spacecraft line is shown. November 24 is DOY 328.

In the tomographic analysis shown here, density and solar wind speed is changed in an iterative fashion to fit brightness and UCSD IPS velocity observations. At the end of each density change and each solar wind velocity change, the three-dimensional solar wind model is recalculated. In order that several different perspective lines of sight reconstruct the model values, we require that more than one line of sight contribute to each latitudinal and longitudinal source surface resolution element in order that it is changed. The tomography program iterates to a solution, generally converging to an unchanging model within a few iterations. In our current analysis the tomographic model is iterated 9 times to a point that few changes occur, and then those lines of sight which do not fit the model to within 3 sigma are removed from the data. The analysis is then iterated for another 9 times to a final answer. Convergence is monitored using several techniques as described in Jackson *et al.*<sup>1</sup> One of the ways used to monitor this convergence is to view the model time series as shown in Fig. 4 for a typical example time series in 1977. Only one of the 128 sectors with observations available approximately every 5 hours is shown. A combination sum of the least square differences between each model and the observed time series gives a criteria that must decrease for the program to register convergence. Tests of the program show that the model solutions are not sensitive to the starting input models, and after a few iterations any signature of the input model is lost. Other tests show that the tomographic technique can reproduce simulated heliospheric structures from remote sensing data using these structures as input.

### 3. HELIOS SPACECRAFT RESULTS AND COMPARISON WITH OTHER DATA

The Helios photometer data both show the way to analyze the data from the Solar Mass Ejection Imager (SMEI), and also yield substantial new scientific information about how CMEs expand and propagate through the interplanetary medium. The basic data from the photometers is brightness time-series information in heliocentric coordinates mapped relative to the Sun. These time series (shown partially for the  $16^\circ$  and  $31^\circ$  photometers in Fig. 1 and for one  $16^\circ$  photometer in Fig. 4) have had a zodiacal light model<sup>16</sup> removed and stellar signals eliminated. To further refine these time series for use with the tomography, we remove an 8-day running mean as in Fig. 4. This filter removes a portion of the low-frequency response not otherwise accounted for. At this level, the Helios systems act as differential photometers for high-frequency heliospheric signals. In addition, the final time series is searched for “glitches”. These

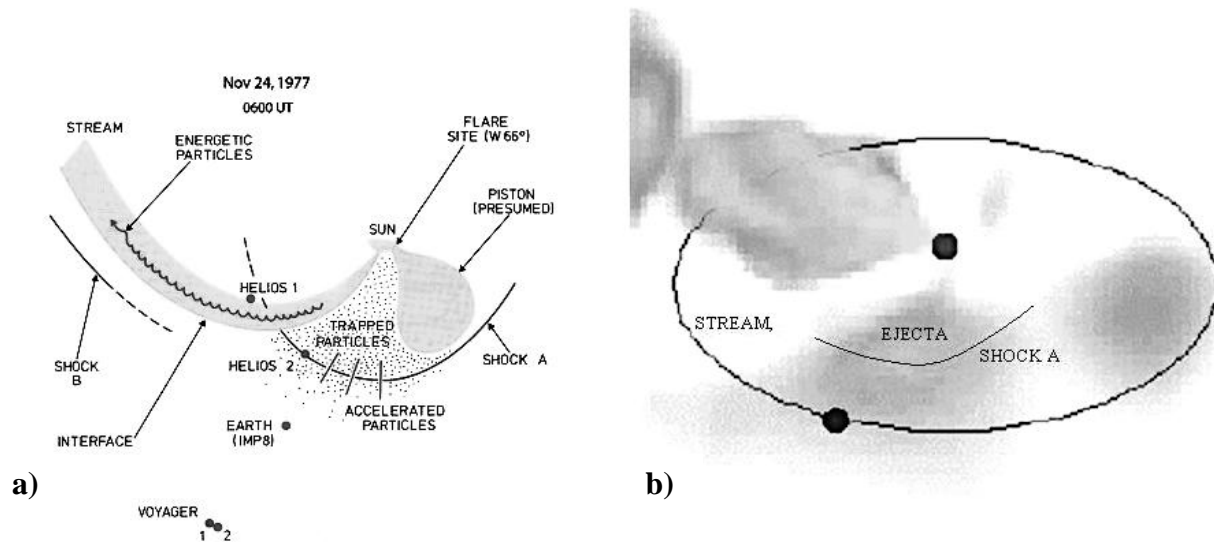


Fig. 5. Nov 24, 1977 time period reconstruction **a)** using *in situ* observations from 5 spacecraft<sup>17</sup>. **b)** Using the IPS time-dependent tomography. Reconstruction on November 24 at 6 UT.

generally appear as spikes in the data that are more prominent above the background in the direction opposite the Sun. These spikes are often correlated with high-energy particle flux observed in the Helios particle detectors<sup>11</sup>. When these spikes are detected in the photometer data, the whole period of time from the Helios photometers is considered suspect and eliminated from consideration even though the high-energy particle spike is not prominent in the photometer observations nearer the Sun. Just such a spike has been removed at DOY 326 from the time series shown in Fig. 4.

Because the very bright zodiacal light component is inseparable from the heliospheric time series signal except by its rapid (less than ~8-day) variation over time, the tomographic analysis must deal with the fact that there is a steady background Thomson-scattering signal component as well as the time-varying one. Several techniques have been devised to include an estimate of this signal in our Thomson-scattering analysis. One of the first methods was to simply analyze the variations relative to the mean datum formed by the running 8-day average<sup>2</sup>. After the 3-D analysis was complete, a small additional  $r^{-2}$  density was added to the data to provide a total density at 1 AU commensurate with the mean value for that time interval at Earth. In the current tomographic analysis shown here, an additional  $r^{-P}$  density with a constant value at 1 AU is added to the model data prior to the tomographic analysis. The sum of the modeled background brightness and the variable component above the mean datum are now compared with total modeled brightness from the three-dimensional model. The Helios spacecraft densities (rather than those at Earth) are now also compared over the time interval in question with the densities derived by our model in order to provide a best interval fit to the value of  $P$  and the density at 1 AU. For the period of time during May 1979,  $P$  was found to be 2.07 with a density at 1 AU of  $7.0 \text{ e}^- \text{ cm}^{-2}$ . For a less active time in 1977 (Carrington rotation 1653)  $P$  was found to be ~2.10 with a 1 AU value of  $8.5 \text{ e}^- \text{ cm}^{-2}$ . The different techniques used in background density fitting make little difference in the location of the heliospheric structures reconstructed, but they do somewhat change the overall density.

Once a three-dimensional result is available, it can be viewed from any perspective or extrapolated to any position in space. Fig. 5a is a graphic depiction of a period in November 1977 that has been well studied using *in situ* data from 5 different spacecraft<sup>17</sup>. Fig. 5b is a remote observer view of the Helios data at this same time period. The Helios photometer tomographic model density satisfactorily depicts both the corotating structure and the assumed CME piston that were studied using *in situ* observations.

The major structure observed in Fig. 6 is a coronal mass ejection (CME) that was observed by the Solwind coronagraph<sup>18</sup> to arise from the Sun to the solar northwest at midday 7 May, 1979. This well-studied CME<sup>12,13,19,20</sup> was termed “three-pronged” by the Solwind coronagraph group. At the time of Fig. 7 the front portion of the CME is estimated to have a solar distance of ~1.0 AU<sup>19</sup>. Poland *et al.*<sup>18</sup> estimate that this CME had an excess mass of  $10^{16}$  g assuming that its entire excess mass was located in the plane of the sky observed by Solwind. The CME underwent considerable evolution by the time it reached the Helios viewing position, expanding both outward and in north-south size. By summing over time

and space in the 3-D matrix using the current tomographic reconstruction, this CME is estimated to have an excess mass of  $\sim 4 \times 10^{16}$  g at 1.0 AU. If the total CME mass above zero within the CME volume is included, the CME mass is estimated to be  $\sim 1 \times 10^{17}$  g and the CME takes from 18 UT 9 May to 18 UT 13 May, 1979 to completely pass 1 AU! This compares with values of  $6 \times 10^{15}$  g and  $9 \times 10^{15}$  g respectively for the outer portion of this CME obtained by the two-spacecraft tomographic reconstruction technique<sup>20</sup>. The two-spacecraft technique shows approximately the same type structure reconstructed. In the 3-D reconstruction techniques, the northern portion of the CME is directed away from Earth and northerly while the southern feature is directed primarily northwest of the Sun-Earth line.

Fig. 8 is a Carrington synoptic map of heliospheric density 1.0 AU at 12 UT on 10 May 1979 obtained from the Helios 2 photometer data. Since only Helios 2 photometer observations are used, there is no data coverage at southern heliographic latitudes and the model leaves these areas blank. The remote-observer view (Fig. 7) of northern heliospheric density shows the heliospheric manifestation of the 7 May 1979 CME (Jackson *et al.*<sup>19</sup>, Fig. 4) at the same time as the 1 AU Carrington map of Fig. 8. Fig. 9 is a comparison plot of heliospheric density at the Helios 2 spacecraft and the reconstructed density in the time-dependent kinematic model extracted at the location of the spacecraft. The *in situ* density values at Helios 2 are averaged using an 18-hour filter in order that they have the same approximate temporal resolution as the  $10^\circ \times 10^\circ$  daily spatial model.

The 1979 time period during Carrington rotation 1681 is at the extreme maximum of CME activity for Solar Cycle 21. Far more CMEs can be observed throughout this period and related to CMEs observed by the Solwind coronagraph, and some of these CMEs and CME sequences are far more massive than the single isolated 7 May CME. In particular this is the case with a CME that erupted from the Sun on 25 May 1979. A more complete data set and a video of over 40 days of this northern hemisphere Helios 2 reconstruction of heliospheric density can be found on the Web at: <http://casswww.ucsd.edu/solar/tomography/>. An additional video sequence and images of an earlier (and less active) temporal interval (Carrington rotation 1653, in the year 1977) can be found at the same location. In this sequence, both Helios 1 and Helios 2 photometer data are used in the reconstruction of northern and southern heliospheric features, and both corotating and CME structures can be observed in the remote-observer views. The correlation with Helios 2 densities for the entire 1653 Carrington rotation is 0.86.

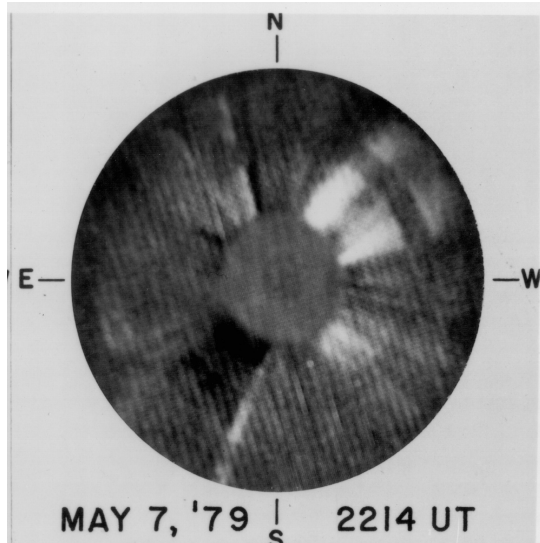
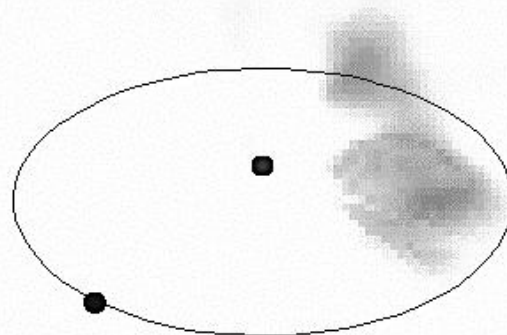


Fig. 6: Solwind coronagraph image of the 7 May CME observed at the time indicated. The coronagraph outer field of view extends to  $8 R_S$ .



CASS/UCSD 1979/05/10 12

Fig. 7: Remote observer view of heliospheric density at the time indicated. An  $r^{-2.07}$  density gradient fit to the observations over the Carrington rotation 1681 interval has been removed from the kinematic model ambient (fit from Helios 2 *in situ* measurements at  $7.0 \text{ e}^- \text{ cm}^{-2}$  at 1 AU), and to the reconstructed structures to aid in viewing them. The observer is located at 3.0 AU  $30^\circ$  above the ecliptic plane  $\sim 45^\circ$  west of the Sun-Earth line.

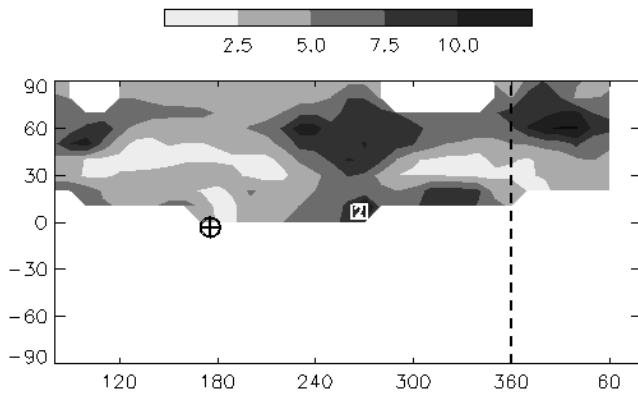


Fig. 8: Carrington synoptic map of heliospheric structure at 1.0 AU at 12 UT 10 May 1979. At this time the Helios 2 spacecraft is  $\sim 90^\circ$  west of Earth in heliographic longitude (indicated) at a solar distance of 0.3 AU.

#### 4. CONCLUSIONS

The tomographic analysis handles density both nearby and distant from the spacecraft as accurately as the modeling and data precision allow. We continue to upgrade our tomographic analysis techniques as newer solar wind models are incorporated. In particular, the simple kinematic model currently used in the reconstruction is somewhat crude, and we expect to replace this (or provide an alternate iterative sequence) with a more precise model such as 3D-MHD that can be used in the tomography. Primarily data quantity, precision, and computational convenience restrict spatial and temporal resolution of the heliospheric structures that are reconstructed. The Solar Mass Ejection Imager (SMEI)<sup>21-26</sup> will be able to reconstruct density over the entire heliosphere with approximately  $1^\circ \times 1^\circ$  heliospheric latitude-longitude spatial resolution and a 90-minute temporal cadence. Although structures near the Earth can be more accurately reconstructed than can those more distant from it, we expect that other instruments (STEREO) may operate during the same times as SMEI. If so these other instruments may help fill in heliospheric regions not observed well from the spacecraft in order to help complete the SMEI far-field view.

#### ACKNOWLEDGEMENTS

The work of B.V. Jackson, P. P. Hick and A. Buffington was supported at the University of California at San Diego by AFOSR grant F49620-01-1-0054 by subcontract F19628-00-C-0029 from the U.S. Air Force and NASA grants NAG5-8504 and NAG5-9423.

#### REFERENCES

1. B.V. Jackson, P.L. Hick, M. Kojima, and A. Yokobe, "Heliospheric tomography using interplanetary scintillation observations, 1. Combined Nagoya and Cambridge data", *J. Geophys. Res.* **103 (A6)**, pp. 12049-12068, 1998.
2. B.V. Jackson, and P. Hick, "Three dimensional tomography of heliospheric features using global Thomson scattering data", *Advances Space Research*, **25 (9)**, pp. 1875-1878, 2000.
3. D.C. Wilson, *NCAR Cooperative Thesis No. 40*, Ph.D. thesis to the University of Colorado, Boulder, Colorado, 1977.
4. B.V. Jackson, "A coronal hole equatorial extension and its relation to a high speed solar wind stream", *Topical Conference on Solar and Interplanetary Physics*, Tucson, Arizona, pp. 7-10, 12-15 January, 1977.

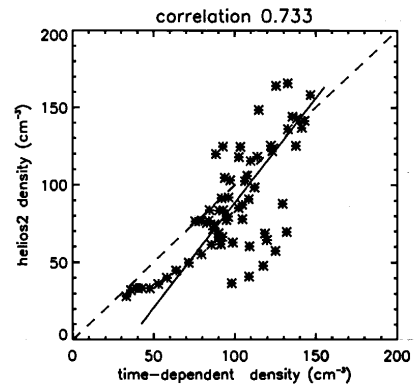
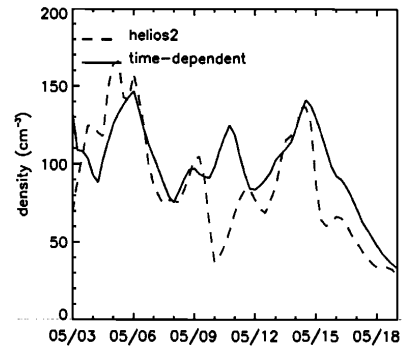


Fig. 9: Comparison plot of heliospheric densities at the Helios 2 spacecraft and least squares correlation.

5. S. Zidowitz, B. Inhester, and A. Epple, "The three-dimensional structure of the solar corona", in *Solar Wind Eight, AIP Conference Proceedings* **382**, edited by D. Winterhalter, J.T. Gosling, S.R. Habbal, W.S. Kurth, and M. Neugebauer, pp. 165-168, Woodbury, 1995.
6. B.V. Jackson, and P. Hick, "Time dependent tomography of heliospheric features using global Thomson-scattering data from the helios spacecraft photometers during times of solar maximum", *EOS*, **81**, p. S353, 18-22 June, 2000.
7. B.V. Jackson, A. Buffington, and P.P. Hick, "A heliospheric imager for solar orbiter", Proc. of "Solar Encounter: The First Solar Orbiter Workshop", Puerto de la Cruz, Tenerife, Spain, 14-18 May 2001 (*ESA SP-493*, September 2001) pp. 251-256, 2001.
8. B.V. Jackson, P.P. Hick and A. Buffington, "Time-dependent tomography of heliospheric features using interplanetary scintillation (IPS) remote-sensing observations," *Proceedings of Solar Wind 10*, Pisa, June 17-21, submitted, 2002.
9. C. Leinert, H. Link, E. Pitz, N. Salm, and D. Knuppelberg, "The Helios zodiacal light experiment (E9)", *Raumfahrtforschung*, **19**, pp. 264-267, 1975.
10. C. Leinert, E. Pitz, H. Link, and N. Salm, "Calibration and in-flight performance of the zodiacal light experiment on Helios", *Space Sci. Instrum.* **5**, pp. 257-270, 1981.
11. I. Richter, C. Leinert, and B. Planck, "Search for short term variations of zodiacal light and optical detection of interplanetary plasma clouds", *Astronomy and Astrophysics*, **110**, (1), pp. 115-120, 1982.
12. B.V. Jackson and C. Leinert, "HELIOS images of solar mass ejections", *J. Geophys. Res.* **90**, pp. 10759-10769, 1985.
13. B.V. Jackson, "Imaging of coronal mass ejections", *Solar Phys.* **100**, pp. 563-575, 1985.
14. B.V. Jackson, "Helios spacecraft photometer observations of elongated corotating structures in the interplanetary medium", *J. Geophysical Research*, **96** (A7), pp. 11,307-11,318, 1991.
15. D.E. Billings, "A guide to the solar corona", p. 150, Academic, New York, July, 1966.
16. C. Leinert, I. Richter, E. Pitz, and B. Planck, "The zodiacal light from 1.0 to 0.3 A.U. as observed by the Helios space probes", *Astronomy and Astrophysics*, **103** (1), pp. 177-188, 1981.
17. L. Burlaga, R. Lepping, R. Weber, T. Armstrong, *et al.*, "Interplanetary particles and fields, November 22 to December 6, 1977: Helios, Voyager, and Imp observations between 0.6 and 1.6 AU", *J. Geophysical Res.*, **85** (A4), pp. 2227-2242, 1980.
18. A.I. Poland, R.A. Howard, M.J. Koomen, D.J. Michels and N.R. Sheeley, Jr, "Coronal transients near sunspot maximum", *Solar Physics*, **69** (1), pp. 169-175, 1981.
19. B.V. Jackson, B. Rompolt, and Z. Svestka, Solar and interplanetary observations of the mass ejection on 7 May 1979, *Solar Physics*, **115** (2), pp. 327-343, 1988.
20. B.V. Jackson, and H.R. Froehling, "Three-dimensional reconstruction of a coronal mass ejection", *Astronomy and Astrophysics*, **299** (3), pp. 885-892, 1995.
21. B.V. Jackson, H.S. Hudson, J.D. Nichols, and R.E. Gold, "Design considerations for a 'solar mass ejection imager' on a rotating spacecraft", in *Solar System Plasma Physics*, J.H. Waite Jr., J.L. Burch and R.L. Moore, eds., *Geophysical Monograph* **54**, pp. 291-297, 1989.
22. B. Jackson, R. Gold, and R. Altrrock, "The Solar Mass Ejection Imager", *Adv. Space Res.* **11**, pp. 377-381, 1991.
23. B.V. Jackson, D.F. Webb, R.C. Altrrock and R. Gold, "Considerations of a solar mass ejection imager in a low-earth orbit", *Eruptive Solar Flares*, Z. Svestka, B.V. Jackson, and M.E. Machado (eds.), Springer-Verlag, Heidelberg, pp. 322-328, 1992.
24. S.L. Keil, R.C. Altrrock, S. Kahler, B.V. Jackson, A. Buffington, P.L. Hick, G.M. Simnett, C.J. Eyles, D. Webb, and P. Anderson, "The solar mass ejection imager (SMEI)", *S.P.I.E. proc.* **2804** pp. 78-89, 1996.
25. S.L. Keil, R.C. Altrrock, S.W. Kahler, B.V. Jackson, A. Buffington, P.L. Hick, G. Simnett, C. Eyles, D.F. Webb and P. Anderson, "The solar mass ejection imager (SMEI): development and use in space weather forecasting", in *Solar Drivers of Interplanetary and Terrestrial Disturbances*, K.S. Balasubramaniam, S.L. Keil and R.N. Smartt eds., ASP Conference Series **95**, pp. 158-166, 1996.
26. B.V. Jackson, A. Buffington, P. Hick, S.W. Kahler, S.L. Keil, R.C. Altrrock, G.M. Simnett, and D.F. Webb, "The solar mass ejection imager", *Phys. Chem. Earth* **22**, pp. 441-444, 1997.

---

\* bvjackson@ucsd.edu; phone 858-534-3358; fax: 858-534-2294

\*\* pphick@ucsd.edu; phone 858-534-8965; fax: 858-534-0177

\*\*\* abuffington@ucsd.edu; phone 858-534-6630; fax: 858-534-7051; <http://casswww.ucsd.edu/solar/smei/index.html>; mail code 0424, UCSD, 9500 Gilman Drive, La Jolla, CA 92093-0424